Phase Calibration of Liquid-Crystal-Based Spatial Light Modulators Using the Spatial Structure of Focused Optical Fields

L. Turquet,* M. Kauranen, and G. Bautista†
Photonics Laboratory, Physics Unit, Tampere University, P. O. Box 692, FI-33014 Tampere, Finland

(Received 6 February 2019; revised manuscript received 13 March 2019; published 16 April 2019)

We present an *in situ* microscopic technique to calibrate phase-only liquid-crystal-based spatial light modulators (LC SLM). The technique relies on the spatial structure of focused fields that are commonly encountered in optical microscopy. To retrieve the phase response curve of the LC SLM, we modulate the phase of one half of the incident beam, record the resulting variations of the focused fields at the focal plane of the microscope objective, and perform a correlation of those variations in the corresponding experimental and theoretical intensity distributions of the focused fields. We establish the validity of the technique by comparing its performance to the well-known two-beam interference technique for calibrating a phase-only LC SLM. Our technique is general, robust, and directly applicable to any microscopy set up that utilizes a LC SLM in the excitation path.

DOI: 10.1103/PhysRevApplied.11.044050

I. INTRODUCTION

Spatial light modulators (SLMs) are very useful and versatile components for wavefront shaping applications. For example, SLMs have been used in micromanipulation [1,2], beam shaping [3,4], microfabrication [5,6], vector field generation [7,8], microscopy [9], quantum optics [10], nonlinear optics [11,12], and many others. Such applications often utilize pixelated phase-only liquid-crystal-based spatial light modulators (LC SLMs) that are typically addressed with a two-dimensional (2D) matrix with 8-bit precision, that is, with 256 levels, whose relationship to the resulting phase delay is unknown. The desired range of phase delays and the mapping of LC SLM input levels to this range of phase delays is to be found. Although manufacturers of LC SLM provide typical phase response curves, calibration within the set up itself is still necessary before proper use or modification of the initial factory settings.

Several techniques have already been developed to calibrate the phase response of LC SLMs. Many of these techniques rely on interferometric approaches [13–16], requiring the generation of interference fringes between phase-modulated and unmodulated beams and subsequent phase retrieval. Although such techniques are reliable and well established, they are very sensitive to environmental disturbances. To remedy the above issue in the LC SLM phase calibration, common-path interferometry has been developed [17,18]. Alternatively, other phase calibration techniques, which rely on diffraction, have been developed [19–22]. Here, the phase response curve of the LC SLM is retrieved by measuring the variations in the intensities of the resulting diffraction-limited spots, which are produced by a set of simple holograms, for example, binary gratings, on the LC SLM. These techniques, however, are still prone to residual intensity modulation such as zero-order diffraction that arises from the inactive regions between the LC SLM pixels [19].

Here, we introduce an alternative diffraction-based *in situ* technique to calibrate the phase response of a LC SLM. This technique is based on the well-established and naturally encountered spatial structure of the focused fields in optical microscopy [23,24]. To retrieve the phase response curve of the LC SLM, we modulate the phase of one half of the incident beam and correlate the variations in the corresponding experimental and theoretical intensity distributions of the resulting focal fields. The validity of the technique is established by comparing its performance to the well-known two-beam interference technique for calibrating phase-only LC SLMs. The accuracy of the alternative approach is found to be better than 0.2 rad. The technique shows great potential for *in situ* and global calibration of phase-only LC SLMs that are already placed in the excitation path of microscopy set ups.

II. METHODOLOGY

A. Optical microscopy set up

A reflective phase-only LC SLM (Hamamatsu model X10468-07 with the following specifications: 8-bit system, 792×600 pixels, input wavelength range from 620 nm to 1100 nm, 20-μm pixel pitch, and 98% fill factor) is used. The LC SLM is connected to its graphic controller, the

*leo.turquet@tuni.fi
†godofredo.bautista@tuni.fi

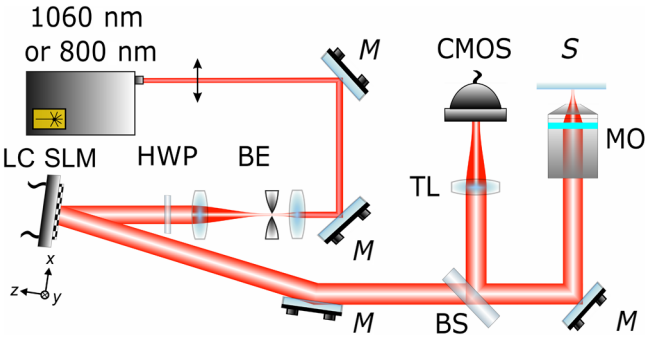

FIG. 1. Schematic diagram of the optical microscopy set up with a LC SLM in the excitation path. Other components: laser (1060-nm or 800-nm excitation wavelength), mirror (M), beam expander (BE), half-wave plate (HWP), beam splitter (BS), microscope objective (MO), microscopy glass slide (S), tube lens (TL), and camera (CMOS). The polarization direction of the incident beam on the LC SLM is indicated by the black double-headed arrow.

latter is connected to a computer, and placed in the excitation path of the optical microscopy set up (Fig. 1). The full details of the optical microscopy set up can be found elsewhere [12,25,26]. Briefly, the microscopy set up is powered by a pulsed laser (1060-nm or 800-nm wavelength, 140-fs pulse duration, 80-MHz repetition rate, and average power of 500 μW when reaching the LC SLM surface). The beam is spatially cleaned, expanded, and directed to the LC SLM. The linearly polarized output of the laser is adjusted carefully using a half-wave plate (HWP) in order to accurately match the director of the liquid crystal molecules of the LC SLM and, more importantly, to avoid any unwanted residual amplitude modulation. The angle of incidence on the LC SLM is less than 10°. The incident angle below 10° is recommended by the company and is not expected to produce depolarization of the reflected light that is usually significant at high incident angles [27]. The beam reflected from the LC SLM is then directed to a microscope objective (Nikon CFI LU Plan Fluor Epi P 50X N.A. 0.80/W.D. 1.0 mm, infinity corrected, semiapochromat, 50× magnification, numerical aperture of 0.8). The intensity distribution of the reflected light from the glass slide (S) is collected using the same objective in combination with the correct tube lens (LA1708, Thorlabs, plano-convex, $f = 200$ mm, uncoated) and viewed with a camera (Compact USB 2.0 CMOS Camera, Thorlabs, resolution of 1280 × 1024 pixels, 5.2 × 5.2 μm^2 pixel size).

It should be made clear that only the illuminated area of the LC SLM is calibrated. The dimension of the illuminated area is generally dictated by the size (or shape) of the input beam. In our microscopy experiments, the size (shape) of the expanded input beam to the SLM is around 6 mm (circular), which covers about 71 000 pixels. Furthermore, the illuminated area is chosen to be near the center of the 15.8 × 12 mm^2-sized rectangular aperture of the LC SLM since the deviations that arise from surface distortions are usually highest near the corners of the LC SLM. One could, in principle, also expand the beam to cover even more pixels.

B. Basis of phase calibration technique

Our technique relies on phase modulation of one half of the beam, subsequent experimental recording of the varying focal-field intensities, and performing a correlation of those variations in the corresponding experimental and theoretical intensity distributions of the focused fields. First, the full LC SLM aperture (792 × 600 pixels) is artificially divided into two symmetric subapertures (396 × 600 pixels) where each one is assigned to one half of the input beam as seen in Fig. 2(a). Due to the incident polarization requirement, which is assumed to be horizontal and aligned to the director of the LC molecules, the aperture of the LC SLM can only be artificially divided in the top-down or left-right subaperture divisions. For our demonstration, we use the left-right subaperture divisions. While the LC SLM input phase delay of the left subaperture is fixed to 0, the input phase delay of the right subaperture is varied between 0 and 2π.

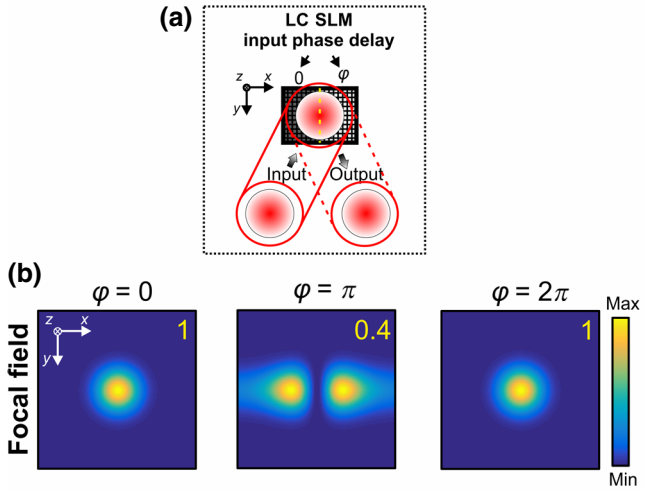

FIG. 2. (a) Schematic of the idea. A Gaussian beam, which is linearly-polarized along x, is incident on the LC SLM. The beam is ensured to fall near the center of the LC SLM. The full aperture of the LC SLM is artificially divided into two equal (left and right) subapertures. For the left subaperture, the input phase delay (φ) is set to 0. For the right sub-aperture, φ is varied from 0 to 2π. (b) Simulated focal-field intensities at the focal plane (x, y, $z = 0$) of the microscope objective (numerical aperture of 0.8) for different phase delays between the two sections of the input beam. The input Gaussian beam is linearly polarized along x. The excitation wavelength (λ) is 1060 nm and the environment is air. The relative intensity levels are shown at the top-right corner of each image for comparison, the reference being the focal-field intensity for 0 delay (leftmost column).

The theoretical intensity distributions right after the LC SLM and at the focal plane of the microscope objective (numerical aperture of 0.8) for an x polarized Gaussian input beam and excitation wavelength of 1060 nm are calculated [Fig. 2(b)]. The theoretical intensity distributions at the focal plane are obtained using direct Fourier transform of the input Gaussian beam with 256 linearly spaced phase delays between 0 and 2π applied over half of the beam. Here, the term phase delay refers to the phase difference between the reflected light from the left and right subapertures of the LC SLM. The computation is performed using the discrete Fourier transform function *fft2* of MATLAB. The paraxial approximation is assumed. For tight focusing configurations, a full vectorial description of the input beam is expected to improve the accuracy of the technique. As seen in Fig. 2(b), when the phase delay on the right subaperture is set to 0 or 2π, the theoretical intensity distributions at the focal plane are found to be equivalent, consisting of a single on-axis lobe as expected. On the other hand when the phase delay on the right subaperture is set to π, the theoretical intensity distribution at the focal plane consists of two off-axis lobes [24]. It should be noted that the application of the same phase delays on both sides of the input beam did not change the theoretical focal-field intensity distributions.

In the experiment, the LC SLM input level of the right subaperture is varied between 0 and 255 with an increment of 1, while the LC SLM input level of the left subaperture is fixed to 0. The LC SLM input level of the right subaperture is gradually increased every 0.5 s. In parallel, a video of the focal-field intensities is simultaneously recorded using the CMOS camera. The frame rate of detection is set to be at least two times higher than the interval of change between two LC SLM input levels. Also, some LC SLM input level increments higher than 1 might be required, especially on low LC SLM input levels, to see intensity variations. However, it should be noted that increasing phase delays lead not only to changes in intensity values, but also in the spatial intensity distribution, which are both taken into account in the correlation process. The recorded video of the focal-field intensities, which is a function of LC SLM input levels from 0 to 255, is postprocessed using MATLAB. In addition, only a small region of interest of the whole image frame where the focal fields are visible (100×100 pixels) is utilized. Regarding the spot size, for instance, at $\lambda = 1060$ nm, the FWHM on the CMOS camera is 127 μm, which leads to a 2.5-μm FWHM at focus if we consider a $50\times$ magnification of the objective.

C. Description and implementation of matching algorithm

Next, the variations of the experimental focal-field intensities are correlated to the variations of the theoretical focal-fields distributed between 0 and 2π. The number

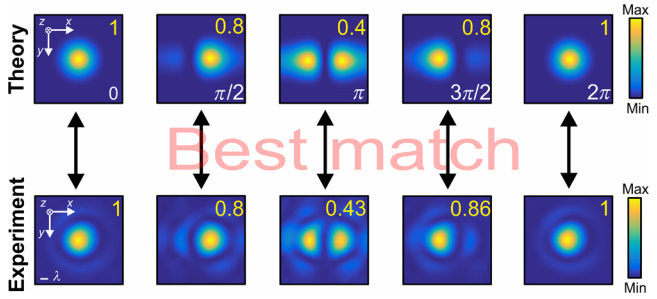

FIG. 3. Theoretical (top row) and experimental (bottom row) focal-field intensities for different phase delays between the two equal sections of the input beam. The input Gaussian beam is linearly polarized along x. Examples of the matching theoretical and experimental images with the highest correlation coefficients are shown. The excitation wavelength (λ) is 1060 nm and the environment is air. The relative intensity levels are shown at the top-right corner of each image for comparison, the reference being the focal-field intensity for 0 delay (leftmost column).

of theoretical intensity distributions we use in the image correlation is the same as the experimental ones, that is to say, 256. These theoretical distributions correspond to 256 linearly spaced phase delays between 0 and 2π that are applied over half of the input Gaussian beam. The lateral dimensions of the theoretical intensity distributions are adjusted and scaled (pixel-wise) in order to match the transverse size of the measured beam obtained at focus for 0 phase delay. The criterion used to match the transverse size of the experimental and theoretical beam distributions at the focal plane is the match of the FWHM values of the main lobe(s) of the experimental and theoretical focal fields. The centering is ensured by matching the maximum of theoretical and experimental distributions for 0 phase delay. These steps are performed in MATLAB. The theoretical and experimental intensity distributions are then normalized according to the maximum intensity value obtained for 0 phase delay. These relative intensity coefficients are shown in Fig. 3.

Considering that a fixed-frame rate ratio between the camera and the LC SLM input level is used, each image frame that is recorded on the camera is precisely related to the corresponding LC SLM input level displayed at that instant. The 2D correlation coefficients between one experimental intensity image and all the simulated images between 0 and 2π are calculated using the built-in *corr2* function of MATLAB. This function computes the correlation coefficient r between two 2D arrays A and B, corresponding, respectively, to the theoretical and experimental intensity distributions in our work. Here, r is given by

$$r = \frac{\sum_m \sum_n (A_{mn} - \bar{A})(B_{mn} - \bar{B})}{\sqrt{\left[\sum_m \sum_n (A_{mn} - \bar{A})^2\right]\left[\sum_m \sum_n (B_{mn} - \bar{B})^2\right]}},$$

where $\bar{A}$ and $\bar{B}$ are the average of all the elements of the arrays A and B. Both A and B have the same number of elements given by $m \times n$. In our case, A corresponds to a theoretical intensity distribution and B to an experimental intensity distribution. The accuracy of this implementation, however, requires a careful alignment of the two arrays as described earlier.

The maximum correlation coefficient and frame index at which this maximum occurs and the frame index used for the correlation are acquired. By finding the best matches, that is, the highest values of the correlation coefficient between experimental and theoretical focal-field distributions, the phase calibration curve of the LC SLM is determined. This generic process is repeated for all 256 LC SLM input levels.

Figure 3 depicts the variations of the theoretical and experimental focal field intensities with increasing phase delay applied on the right side of the Gaussian beam in the far field. It also generally describes the correlation process between the frames, which is used to find the phase curve of the LC SLM with factory settings. Variations of the focal field intensity start from a one-lobe distribution for the phase delay of 0 to a two-lobe distribution for the phase delay of π. For completeness, the corresponding variations in the focal field intensities for the phase delays from π to 2π are also shown.

A curve composed of the frame index where the SLM input level on the x axis and the corresponding index of the matching pair on the y axis is then plotted. Possible phase jumps in the curves occur when the phase delay goes over 2π. After unwrapping the possible jumps and mapping the index of the theoretical image to a phase delay, the measured phase response curve is retrieved. This curve now shows the LC SLM input level on the x axis and imparted phase delay on the y axis.

III. RESULTS AND DISCUSSION

Using our technique, we acquire the phase response curve of the LC SLM with factory settings at the excitation wavelength of 1060 nm (Fig. 4). It is noticeable that the phase response is rather linear with respect to the LC SLM input level. The phase response curve of the LC-SLM at the excitation wavelength of 800 nm without changing the LC SLM configuration is also shown. In order to prove the validity of our technique, the phase response curve of our LC SLM is also acquired using the interferometric approach. Here, the set up as described in Fig. 1 of Ref. [28] is utilized using the same key components (e.g., laser, LC SLM, and camera) of our optical microscopy set up. Briefly, this technique uses interference fringes generated between a reference Gaussian beam and a phase-modulated beam from the LC SLM.

A maximum local deviation of about 0.2 rad is seen between the interferometric method and our technique.

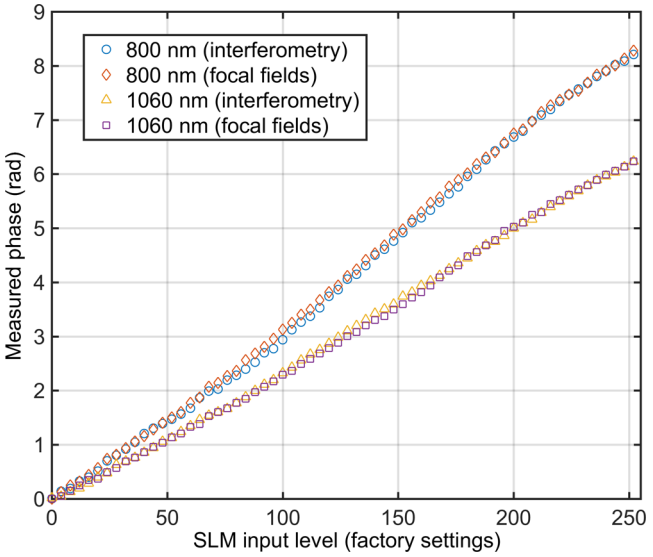

FIG. 4. Measured phase response curves of the LC SLM at its factory default settings obtained using our technique for an input x polarized Gaussian beam at the excitation wavelengths of 1060 and 800 nm. For comparison, the measured phase response curves using the interferometric approach at the wavelengths of 1060 and 800 nm are shown. For better visualization, only 64 out of 256 available data points are shown for each curve.

The standard deviation values of the relative errors for the 1060- (800-) nm wavelength case is found to be 0.055 (0.051) rad, which is comparable to the accuracy levels of the techniques presented in Refs. [16] and [19]. These deviations between the two techniques can be attributed to (1) asymmetries in the spatial structure of the input laser beam, (2) full vectorial focal-field effects as a consequence of tight focusing [29], which were not taken into account in the predictions, and (3) slight mismatches in the scaling and alignment parameters in the correlation algorithm. Finally, although the spot size of the focused light is generally affected by the excitation wavelength (at a fixed numerical aperture of microscope objective and environment), the general behavior of the spatial structure of the focused fields is expected to remain the same. Thus, the technique can be extended, in principle, to obtain the global phase response for any operable wavelength of the LC SLM at high accuracy.

To further illustrate the accuracy of the technique, we perform our calibration technique using theoretical focal fields with FWHM larger or smaller by 25%, 50%, 75%, and 100%, for $\lambda = 1060$ nm. As depicted in Fig. 5, it is evident that the matching of FWHM values between experimental and theoretical focal-field distributions is important, even though the effect is somewhat less important for smaller theoretical FHWM than for larger. Our method thus provides accurate results if the difference of FWHM values between experimental and theoretical intensity

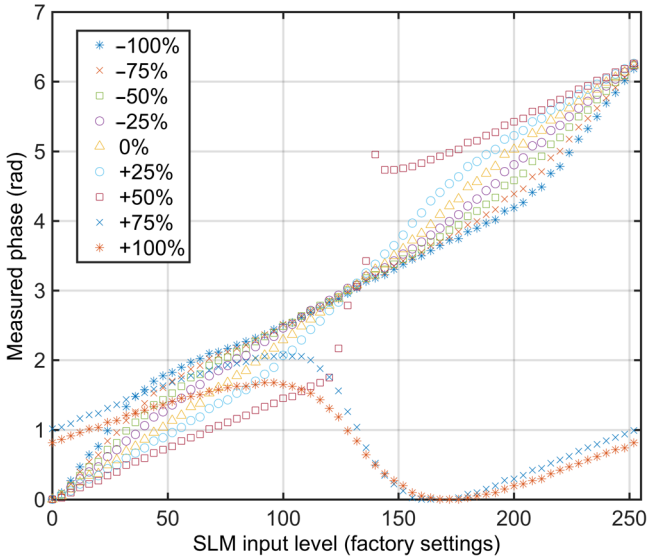

FIG. 5. Effect of smaller and larger FWHMs of the theoretical focal intensity distribution compared to the experimental one, in terms of percentage. The used input wavelength is 1060 nm. For better visualization, only 64 out of 256 available data points are shown for each curve.

distributions is within ±25%. This FWHM matching is, in our case, easily ensured using MATLAB.

It is important to note that the calibrated phase response curves obtained by our technique remain global as they are limited by the number of effective LC SLM pixels that are utilized in the optical microscopy set up. Therefore, the effect of the locally varying phase responses from individual pixels are not accounted for [14,16,28,30]. In the future, we plan to address the role of spatially varying phase responses by parallelizing the technique using spatially multiplexed beams. In this possible extension, an array of linearly polarized Gaussian beams (i.e., beamlets) covering several smaller areas on the SLM can be simultaneously utilized. Such beamlets can then be focused using the microscopy set up and subsequent phase calibration can be performed in parallel, that is, using the same algorithm presented in this work. Regarding the speed of our technique, it is relatively faster than the interferometric approach, as our technique is *in situ,* and therefore, does not require the building of the extra interferometric set up. In terms of data collection and computation, the speed is comparable with existing techniques, as similar steps need to be performed (e.g., in data acquisition and postprocessing) using the interferometric technique or our calibration technique.

IV. CONCLUSIONS

We present an *in situ* microscopic technique to calibrate a phase-only LC SLM. The technique relies on the general spatial structure of focused fields that are commonly encountered in optical microscopy. To retrieve the global phase response curve of the LC SLM, we modulate the phase of one half of the incident beam, record the resulting variations of the focused fields at the focal plane of the microscope objective, and perform a correlation of those variations in the corresponding experimental and theoretical intensity distributions of the focused fields. The validity of the technique is established by comparing its performance to the well-known two-beam interference technique for calibrating a phase-only LC SLM. The technique is found to be general, robust, and directly applicable to any microscopy set up that utilizes a LC SLM in the excitation path. In the future, we also foresee the technique to be useful in performing nonglobal, that is, localized phase calibration.

ACKNOWLEDGMENT

Authors acknowledge the financial support of Academy of Finland (Grants No. 267847 and No. 287651), and PREIN flagship funding (Grant No. 320165). L.T. acknowledges the financial support from the Graduate School of TUT. Authors also thank Hamamatsu Photonics NORDEN AB for the LC SLM loan.

[1] D. G. Grier, A revolution in optical manipulation, Nature **424**, 810 (2003).
[2] R. Lynge Eriksen, V. Ricardo Daria, J. Glückstad, R. Eriksen, V. Daria, and J. Gluckstad, Fully dynamic multiple-beam optical tweezers, Opt. Express **10**, 597 (2002).
[3] N. Chattrapiban, E. A. Rogers, D. Cofield, W. T. Hill III, and R. Roy, Generation of nondiffracting Bessel beams by use of a spatial light modulator, Opt. Lett. **28**, 2183 (2003).
[4] H. Ono, H. Wakabayashi, T. Sasaki, A. Emoto, T. Shioda, and N. Kawatsuki, Vector holograms using radially polarized light, Appl. Phys. Lett. **94**, 071114 (2009).
[5] G. Bautista, M. J. Romero, G. Tapang, and V. R. Daria, Parallel two-photon photopolymerization of microgear patterns, Opt. Commun. **282**, 3746 (2009).
[6] P. Kunwar, L. Turquet, J. Hassinen, R. H. A. Ras, J. Toivonen, and G. Bautista, Holographic patterning of fluorescent microstructures comprising silver nanoclusters, Opt. Mater. Express **6**, 946 (2016).
[7] M. R. Beversluis, L. Novotny, and S. J. Stranick, Programmable vector point-spread function engineering, Opt. Express **14**, 2650 (2006).
[8] J. A. Davis, D. E. McNamara, D. M. Cottrell, and T. Sonehara, Two-dimensional polarization encoding with a phase-only liquid-crystal spatial light modulator, Appl. Opt. **39**, 1549 (2000).
[9] C. Maurer, A. Jesacher, S. Bernet, and M. Ritsch-Marte, What spatial light modulators can do for optical microscopy, Laser Photonics Rev. **5**, 81 (2011).
[10] J. Leach, B. Jack, J. Romero, A. K. Jha, A. M. Yao, S. Franke-Arnold, D. G. Ireland, R. W. Boyd, S. M. Barnett, and M. J. Padgett, Quantum correlations in optical

angle-orbital angular momentum variables, Science (80). **329**, 662 (2010).
[11] V. R. Daria, C. Stricker, R. Bowman, S. Redman, and H.-A. Bachor, Arbitrary multisite two-photon excitation in four dimensions, Appl. Phys. Lett. **95**, 093701 (2009).
[12] L. Turquet, J.-P. Kakko, X. Zang, L. Naskali, L. Karvonen, H. Jiang, T. Huhtio, E. Kauppinen, H. Lipsanen, M. Kauranen, and G. Bautista, Tailorable second-harmonic generation from an individual nanowire using spatially phase-shaped beams, Laser Photonics Rev. **11**, 1600175 (2017).
[13] A. Bergeron, J. Gauvin, F. Gagnon, D. Gingras, H. H. Arsenault, and M. Doucet, Phase calibration and applications of a liquid-crystal spatial light modulator, Appl. Opt. **34**, 5133 (1995).
[14] S. Reichelt, Spatially resolved phase-response calibration of liquid-crystal-based spatial light modulators, Appl. Opt. **52**, 2610 (2013).
[15] F. P. Ferreira and M. S. Belsley, Direct calibration of a spatial light modulator by lateral shearing interferometry, Opt. Express **18**, 7899 (2010).
[16] X. Xun and R. W. Cohn, Phase calibration of spatially nonuniform spatial light modulators, Appl. Opt. **43**, 6400 (2004).
[17] G. Rajshekhar, B. Bhaduri, C. Edwards, R. Zhou, L. L. Goddard, and G. Popescu, Nanoscale topography and spatial light modulator characterization using wide-field quantitative phase imaging, Opt. Express **22**, 3432 (2014).
[18] J. L. M. Fuentes, E. J. Fernández, P. M. Prieto, and P. Artal, Interferometric method for phase calibration in liquid crystal spatial light modulators using a self-generated diffraction-grating, Opt. Express **24**, 14159 (2016).
[19] D. Engström, G. Milewski, J. Bengtsson, and S. Galt, Diffraction-based determination of the phase modulation for general spatial light modulators, Appl. Opt. **45**, 7195 (2006).
[20] Z. Zhang, G. Lu, and F. T. S. Yu, Simple method for measuring phase modulation in liquid crystal televisions, Opt. Eng. **33**, 3018 (1994).
[21] L. Martínez-León, Z. Jaroszewicz, A. Kołodziejczyk, V. Durán, E. Tajahuerce, and J. Lancis, Phase calibration of spatial light modulators by means of Fresnel images, J. Opt. A: Pure Appl. Opt. **11**, 125405 (2009).
[22] C. Doñate-Buendía, G. Mínguez-Vega, J. Lancis, J. Pérez-Vizcaíno, L. Martínez-León, M. Fernández-Alonso, M. Carbonell-Leal, and O. Mendoza-Yero, Diffraction-based phase calibration of spatial light modulators with binary phase fresnel lenses, J. Disp. Technol. **12**, 1027 (2016).
[23] G. Bautista and M. Kauranen, Vector-field nonlinear microscopy of nanostructures, ACS Photonics **3**, 1351 (2016).
[24] L. Novotny, E. J. Sánchez, and X. Sunney Xie, Near-field optical imaging using metal tips illuminated by higher-order Hermite-Gaussian beams, Ultramicroscopy **71**, 21 (1998).
[25] G. Bautista, C. Dreser, X. Zang, D. P. Kern, M. Kauranen, and M. Fleischer, Collective effects in second-harmonic generation from plasmonic oligomers, Nano Lett. **18**, 2571 (2018).
[26] L. Turquet, X. Zang, J.-P. Kakko, H. Lipsanen, G. Bautista, and M. Kauranen, Demonstration of longitudinally polarized optical needles, Opt. Express **26**, 27572 (2018).
[27] A. Lizana, N. Martín, M. Estapé, E. Fernández, I. Moreno, A. Márquez, C. Iemmi, J. Campos, and M. J. Yzuel, Influence of the incident angle in the performance of Liquid Crystal on Silicon displays, Opt. Express **17**, 8491 (2009).
[28] J. Otón, P. Ambs, M. S. Millán, and E. Pérez-Cabré, Multipoint phase calibration for improved compensation of inherent wavefront distortion in parallel aligned liquid crystal on silicon displays, Appl. Opt. **46**, 5667 (2007).
[29] B. Richards and E. Wolf, Electromagnetic diffraction in optical systems. II. Structure of the image field in an aplanatic system, Proc. R. Soc. Lond. Ser. A **253**, 358 (1959).
[30] D. Engström, M. Persson, J. Bengtsson, and M. Goksör, Calibration of spatial light modulators suffering from spatially varying phase response, Opt. Express **21**, 16086 (2013).